Uncovering a membrane-distal conformation of KRAS available to recruit RAF to the plasma membrane

Que N. Van[a], Cesar A. López[b], Marco Tonelli[c], Troy Taylor[a], Ben Niu[d,1], Christopher B. Stanley[e], Debsindhu Bhowmik[e], Timothy H. Tran[a], Peter H. Frank[a], Simon Messing[a], Patrick Alexander[a], Daniel Scott[f,2], Xiaoying Ye[a,2], Matt Drew[a], Oleg Chertov[a], Mathias Lösche[f,g,h], Arvind Ramanathan[i], Michael L. Gross[d], Nicolas W. Hengartner[b], William M. Westler[c], John L. Markley[c], Dhirendra K. Simanshu[a], Dwight V. Nissley[a], William K. Gillette[a], Dominic Esposito[a], Frank McCormick[a,3], S. Gnanakaran[b], Frank Heinrich[g,h], and Andrew G. Stephen[a,3]

[a]National Cancer Institute RAS Initiative, Cancer Research Technology Program, Frederick National Laboratory for Cancer Research, Leidos Biomedical Research, Inc., Frederick, MD 21702; [b]Theoretical Biology and Biophysics Group, Los Alamos National Laboratory, Los Alamos, NM 87545; [c]National Magnetic Resonance Facility at Madison, Biochemistry Department, University of Wisconsin–Madison, Madison, WI 53706; [d]National Mass Spectrometry Resource, Department of Chemistry, Washington University in St. Louis, St. Louis, MO 63130; [e]Computational Sciences and Engineering Division, Oak Ridge National Laboratory, Oak Ridge, TN 37831; [f]Department of Biomedical Engineering, Carnegie Mellon University, Pittsburgh, PA 15213; [g]Department of Physics, Carnegie Mellon University, Pittsburgh, PA 15213; [h]Center for Neutron Research, National Institute of Standards and Technology, Gaithersburg, MD 20899; and [i]Data Science and Learning Division, Argonne National Laboratory, Lemont, IL 60439

Contributed by Frank McCormick, July 20, 2020 (sent for review April 13, 2020; reviewed by Matthias Buck and Roland Winter)

The small GTPase KRAS is localized at the plasma membrane where it functions as a molecular switch, coupling extracellular growth factor stimulation to intracellular signaling networks. In this process, KRAS recruits effectors, such as RAF kinase, to the plasma membrane where they are activated by a series of complex molecular steps. Defining the membrane-bound state of KRAS is fundamental to understanding the activation of RAF kinase and in evaluating novel therapeutic opportunities for the inhibition of oncogenic KRAS-mediated signaling. We combined multiple biophysical measurements and computational methodologies to generate a consensus model for authentically processed, membrane-anchored KRAS. In contrast to the two membrane-proximal conformations previously reported, we identify a third significantly populated state using a combination of neutron reflectivity, fast photochemical oxidation of proteins (FPOP), and NMR. In this highly populated state, which we refer to as "membrane-distal" and estimate to comprise ∼90% of the ensemble, the G-domain does not directly contact the membrane but is tethered via its C-terminal hypervariable region and carboxymethylated farnesyl moiety, as shown by FPOP. Subsequent interaction of the RAF1 RAS binding domain with KRAS does not significantly change G-domain configurations on the membrane but affects their relative populations. Overall, our results are consistent with a directional fly-casting mechanism for KRAS, in which the membrane-distal state of the G-domain can effectively recruit RAF kinase from the cytoplasm for activation at the membrane.

KRAS | membrane | neutron reflectometry | RAF RBD | nuclear magnetic resonance

RAS proteins function as molecular switches that regulate cell growth by oscillating between an inactive guanosine diphosphate (GDP)-bound state and active guanosine triphosphate (GTP)-bound state. Three human genes give rise to four protein isoforms: HRAS, NRAS, and the alternatively spliced variants, KRAS4a and KRAS4b. KRAS is the most frequently mutated isoform, as it is identified in 60% of pancreatic, 33% of colorectal, and 17% of lung cancers (1). While all RAS proteins contain an almost identical G-domain, they vary significantly in their C-terminal hypervariable region (HVR). It is the HVR that undergoes posttranslational modifications and targets RAS to the plasma membrane (2, 3). All RAS isoforms have a bipartite membrane-targeting motif that includes a farnesylated and carboxymethylated terminal cysteine residue in combination with either monopalmitoylated (NRAS and KRAS4a), bipalmitoylated (HRAS), or a polybasic domain (PBD) (KRAS4b). At the plasma membrane, KRAS4b diffuses laterally to form higher-order oligomers or nanoclusters (4, 5), which localize at anionic lipids, particularly phosphatidylserine and phosphatidic acid (6, 7). Lysine residues within the PBD of KRAS4b define the lipid specificity which facilitate the formation of these nanoclusters (8).

Significance

The proto-oncogene *KRAS*, a small GTPase, is frequently mutated in pancreatic, colorectal, and lung cancer. These mutations result in elevated levels of the activated guanosine triphosphate-bound form of KRAS. Localized at the plasma membrane, KRAS functions to recruit effectors, predominantly RAF kinase for activation and initiation of the MAPK signaling cascade. Combining computational and biophysical methods we identify a membrane-distal state of the KRAS G-domain that alternates with two previously described membrane-proximal states through dynamic reorganization of the hypervariable region. Comprising about 90% of the ensemble, this membrane-distal state of the G-domain dominates the proximal states and may facilitate KRAS to recruit cytosolic RAF kinase to the membrane by a fly-casting mechanism.

Author contributions: W.M.W., D.K.S., D.V.N., and D.E. designed research; Q.N.V., M.T., T.T., B.N., T.H.T., P.H.F., S.M., P.A., D.S., X.Y., M.D., O.C., and F.H. performed research; Q.N.V., M.T., B.N., M.L., A.R., M.L.G., W.M.W., D.E., F.M., S.G., F.H., and A.G.S. analyzed data; Q.N.V., C.A.L., T.T., B.N., C.B.S., D.B., S.M., M.L., M.L.G., N.W.H., J.L.M., W.K.G., S.G., F.H., and A.G.S. wrote the paper; C.A.L., C.B.S., and D.B. performed computational work; T.H.T. and D.K.S. provided the X-ray structure; M.L.G., D.V.N., W.K.G., S.G., F.H., and A.G.S. supervised the project; and F.M. contributed to the conception of this work and provided critical feedback on data interpretation.

Reviewers: M.B., Case Western Reserve University; and R.W., TU Dortmund University.

Competing interest statement: F.M. is a consultant for the following companies: Aduro Biotech, Amgen, Daiichi Ltd, Ideaya Biosciences, Kura Oncology, Leidos Biomedical Research, Inc., PellePharm, Pfizer Inc., PMV Pharma, Portola Pharmaceuticals, and Quanta Therapeutics. F.M. has received research grants from Daiichi Ltd, and Gilead Sciences and is a consultant and cofounder for the following companies (with ownership interest including stock options): BridgeBio, DNAtrix Inc., Olema Pharmaceuticals, Inc., and Quartz. F.M. is Scientific Director of the National Cancer Institute RAS Initiative at Frederick National Laboratory for Cancer Research, Leidos Biomedical Research, Inc.

See online for related content such as Commentaries.

[1]Present address: BioPharmaceuticals R&D, AstraZeneca PLC, Gaithersburg, MD 20878.

[2]Present address: Analytical Department, Catalent Pharma Solutions, Gaithersburg, MD 20878.

[3]To whom correspondence may be addressed. Email: frank.mccormick@ucsf.edu or stephena@mail.nih.gov.

This article contains supporting information online at https://www.pnas.org/lookup/suppl/doi:10.1073/pnas.2006504117/-/DCSupplemental.

First published September 10, 2020.

One of the primary downstream targets of KRAS is RAF kinase, which connects RAS activation to the MAPK pathway. Inactive, cytosolic RAF is in an autoinhibited state in which the N-terminal region interacts with the catalytic domain and represses its activity (reviewed in ref. 9). This state is stabilized by the binding of two 14-3-3 proteins to two inhibitory phosphorylation sites (residues Ser259 and Ser621 in RAF1 or CRAF). The recent cryogenic electron microscopy (cryo-EM) structures of the autoinhibited BRAF/14-3-3 and BRAF/MEK1/14-3-3 complexes show the sequestration of the RAF-CRD (RAF cysteine-rich domain) by the 14-3-3 dimer (10, 11). Recruitment of RAF to the plasma membrane, presumably through engagement with RAS nanoclusters, relieves this autoinhibitory state and is therefore required for MAPK signaling (12). While the molecular details of RAF activation remains incomplete, it is clear that binding of the RAF-RBD (RAF RAS binding domain) to RAS allows dephosphorylation of Ser259 by the SHOC2-M-RAS-PP1 complex (13). This causes release of 14-3-3 from the

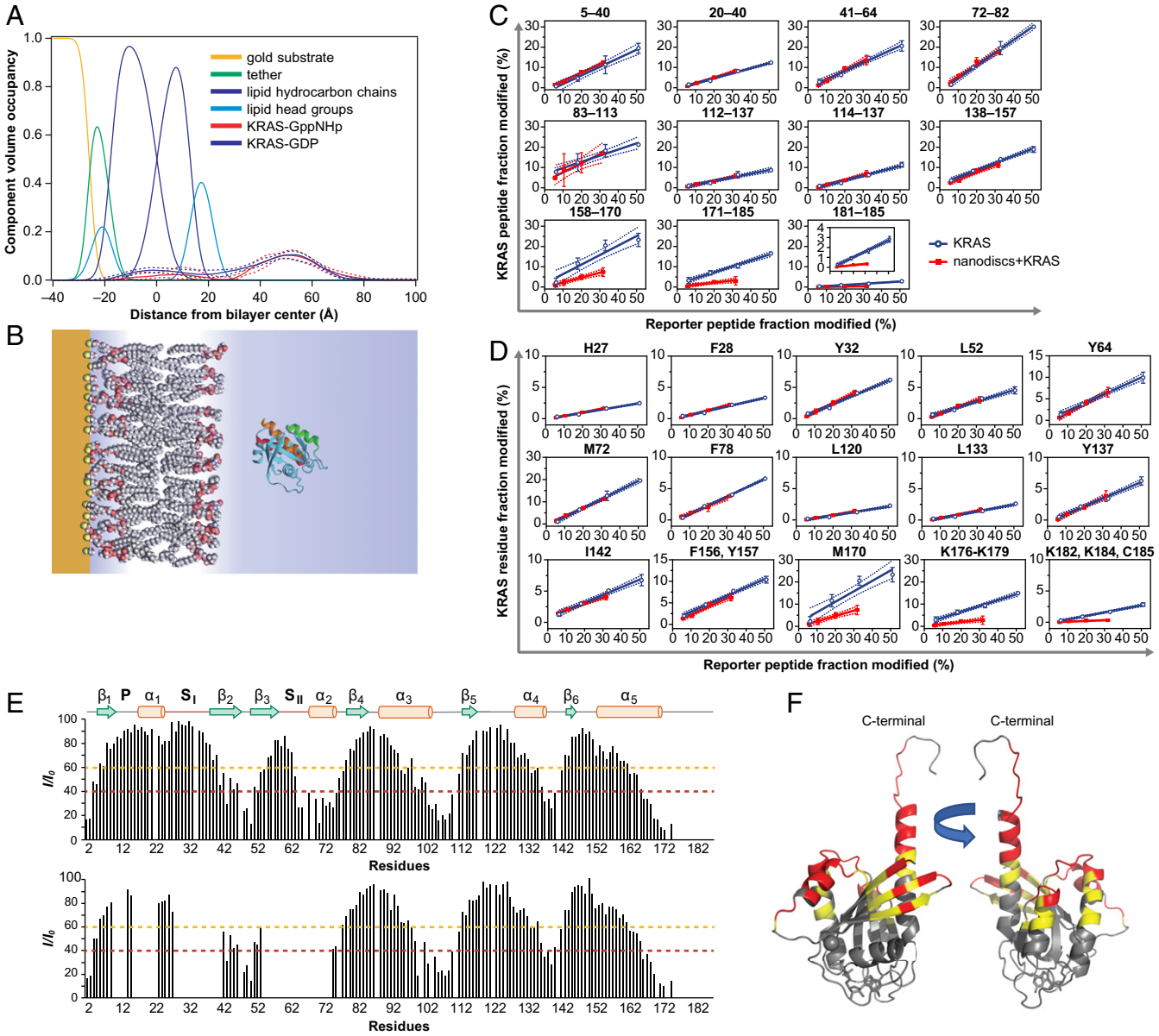

Fig. 1. NR, FPOP, and NMR data of membrane-bound KRAS. (*A*) NR-derived CVO profiles of KRAS-GDP and KRAS-GppNHp associated with 70:30 POPC:POPS stBLMs. The membrane structure shown is from the measurement of KRAS-GppNHp. The KRAS-GDP profile was scaled to match that of KRAS-GppNHp in surface coverage. (*B*) Cartoon of the stBLM-associated KRAS-GppNHp G-domain at a membrane distance in quantitative agreement with the NR results. The orientation of the rotationally symmetric G-domain cannot be determined from the NR data, and an exemplary orientation is shown. Helices α5 (orange ribbon), α4 (green ribbon), and α3 (red ribbon) are highlighted for reference. (*C*) FPOP dose–response curves for various regions of KRAS-GDP as represented by peptides from proteolysis of unbound (blue) and nanodisc-bound (red) protein. The scavenger concentration was varied to change the radical dose to the protein (or the time provided for reaction). Data for each region are plotted as the fraction modified of the representative peptide vs. the fraction modified of the reporter peptide at each histidine (scavenger) concentration. Ninety-five-percent confidence intervals for each curve are shown as shaded regions. (*D*) Residue-level FPOP response curves for nanodisc-bound and unbound KRAS as determined by MS/MS analyses of the peptides. (*E*) NMR-PRE ratios for KRAS-GDP (*Top*) KRAS-GppNHp (*Bottom*) on 70:30 POPC:POPS nanodiscs. Unassigned and excluded residues within the G-domain (2–170) are left blank, see *SI Appendix* for further information. Secondary structure elements are based on predictions from TALOS-N using backbone chemical shifts. (*F*) NMR-PRE ratios (I/I_o) from KRAS-GDP projected onto a model structure at 40% (red) and 60% (yellow) cutoffs.

Ser259 binding site (while the C-terminally bound 14-3-3 protomer remains complexed) and promotes the interaction of RAF-CRD with phosphatidylserine at the plasma membrane. The final step of RAF activation is dimerization, driven by the increase in local RAF concentration at RAS nanoclusters (see ref. 14 for review).

Defining how KRAS4b interacts with the membrane can provide insights on how it recruits and facilitates RAF activation. HADDOCK (High Ambiguity Driven protein–protein DOCKing) studies restrained by NMR paramagnetic relaxation enhancement (NMR-PRE) results for KRAS4b that was chemically tethered to lipid nanodiscs (15) showed that the G-domain populates two membrane-bound conformations that differ in their accessibility of the RBD binding site. Computational methods also support the relevance of these configurations and led to structural models of the membrane-anchored KRAS4b/RAF1–RBDCRD complex (16–18).

The currently available structural information on KRAS membrane association provides important hints to assess its interaction with downstream effectors; however, gaps remain that limit our knowledge of KRAS4b-membrane biology. For instance, the dynamics of transitions between the membrane-associated states of KRAS are not well characterized, and it remains unclear whether its G-domain remains membrane-associated or can dissociate while remaining membrane-tethered via its disordered HVR (residues S171 to C185). We previously developed a protocol to produce farnesylated and methylated KRAS4b (KRAS4b-FMe). This form of KRAS4b recapitulates the processing of the protein in mammalian cells and represents the authentic version of the protein that can be used to study the interaction of KRAS4b with membranes (19).

As presented here, we rigorously combined diverse biophysical experiments with computational simulations to investigate the interaction and dynamics of the authentically processed KRAS4b-FMe protein with membrane in model lipid systems. Our results show that KRAS4b-FMe, hereafter referred to as KRAS, binds at the membrane surface where it is highly dynamic, and a high proportion of the G-domain is fully solvent-exposed while remaining tethered to the membrane via its HVR. Yet, a small subset of the population remains closely bound to the membrane in defined orientations that either expose or occlude the RAF effector binding site. Binding of the soluble RAF1-RBD to membrane-associated KRAS alters the relative populations of these conformations and the dynamics of transitions between them, but not the configurational definitions of these states with respect to the membrane.

Results

Characterization of KRAS Association with Charged Bilayers.

KRAS preferentially associates with anionic membranes. The equilibrium binding of prenylated KRAS to anionic sparsely tethered bilayer lipid membranes (stBLMs) (20) was characterized by surface plasmon resonance (SPR) to identify optimal conditions for the structural analysis using neutron reflectometry (NR). stBLMs composed of 1-palmitoyl-2-oleoyl-glycero-3-phosphocholine (POPC) and 1-palmitoyl-2-oleoyl-sn-glycero-3-phospho-L-serine (POPS) were prepared, and the dissociation constant of KRAS-GDP and KRAS-GppNHp as a function of the molar fraction of POPS in the membrane was determined (*SI Appendix*, Fig. S1 and Table S1). KRAS-GDP and KRAS-GppNHp bound to 70:30 POPC:POPS stBLMs with apparent dissociation constants, $K_D = (0.9 \pm 0.3)$ μM and $K_D = (1.2 \pm 0.2)$ μM, respectively, consistent with previous observations (19, 21–23).

KRAS G-domain is displaced from the membrane as determined with NR. NR was used to structurally characterize proteins associated with stBLMs that are immersed in aqueous solvent. It yields one-dimensional (1D) spatial distributions, expressed as component volume occupancy (CVO) profiles, of stBLM components and membrane-associated protein along the membrane normal (24). CVO profiles thus quantify how much volume within a plane at a certain distance z from the interface is occupied by lipid and protein components. The protein CVO profile is either modeled using a free-form Hermite spline or it is derived from rigid body rotations and translations of an independent high-resolution structure with respect to the membrane (25). As an inherently surface-sensitive technique, NR is blind to protein in the aqueous phase adjacent to the interface, and it has been successfully applied in the past to structurally characterize various lipidated, peripheral membrane proteins (24, 26, 27).

NR experiments were conducted with 70:30 POPC:POPS stBLMs exposed to either 500 nM KRAS-GppNHp or 1 μM KRAS-GDP in buffer containing 150 mM NaCl and 5 mM $MgCl_2$. Fig. 1*A* shows the spline CVO profiles of KRAS-GppNHp and KRAS-GDP on such membranes. Protein surface coverages were determined (28, 29) and yielded one protein per (50 ± 4) lipids for KRAS-GDP (solution concentration: 1 μM) and one protein per (100 ± 10) lipids for KRAS-GppNHp (solution concentration: 0.5 μM), in agreement with the results obtained by SPR. No significant differences between CVO profiles from KRAS-GDP and KRAS-GppNHp were observed. For both samples, the main protein density, attributed to the G-domain, peaks at 33 to 38 Å from the center of the substrate-distal lipid headgroups (Table 1). KRAS CVO profiles did not significantly differ when testing the robustness of the results in measurements with buffers without $MgCl_2$ under variation of ionic strengths (*SI Appendix*, Fig. S2 *A* and *B* and Table S2), although an increased amount of membrane-bound protein was observed at 50 mM NaCl.

To interpret the spline CVO profiles of KRAS in terms of an atomistic structure, one of the NR datasets with KRAS-GppNHp was also analyzed by modeling the protein CVO profile using rigid-body rotations of a high-resolution X-ray structure of the KRAS G-domain (Protein Data Bank [PDB] ID code 6VC8) (*SI Appendix*, Fig. S2*C*) (25). While a specific orientation of the G-domain with respect to the membrane could not be identified due to its nearly spherical overall shape, a Gaussian broadening of the X-ray structure by 5 ± 1 Å rms (13 ± 4 Å full width at half maximum [FWHM]) in addition to the globally applied surface roughness of the carrier substrate was required to describe the data. The peak distance of the rigid-body CVO profile remained in agreement with that of the spline CVO profile reported in Table 1. The broadening indicates a positional flexibility of the G-domain along z that is consistent with occasional contact of the G-domain with the membrane. However, such membrane contacts require a translation of the domain by 10 Å or greater from its average location along z that gives rise to the profile peak. From the observed broadening of the atomistic protein profile, it is estimated that the G-domain occupies a membrane-proximal position only with a weight of $11 \pm 4\%$ in the ensemble of configurations (see *SI Appendix* for details).

Residues within the HVR make persistent membrane contacts as revealed by protein footprinting. Fast photochemical oxidation of proteins (FPOP) (30–32) uses hydroxyl radicals with a lifetime in the microsecond range to determine those regions of KRAS that interact directly with the membrane. The time of the exposure to radicals was varied by using different concentrations of a scavenger, histidine (33, 34). We prepared solutions of KRAS alone or in 1:1 ratio with nanodiscs (70:30 POPC:POPS) for FPOP footprinting and analysis (workflow shown in *SI Appendix*, Fig. S3). For mixtures of proteins free in solution and membrane-bound, FPOP results are a composite between the two signals (35). However, at the protein concentration used in solutions with nanodiscs we expect the unbound fraction to be small (15%), and given that the majority of the KRAS is bound, its signal will dominate the composite signal. The presence of lipids and the membrane scaffold protein may act as hydroxyl scavengers and bias the FPOP results between the two samples. To compensate for such differential scavenging and to track the FPOP labeling time, a reporter peptide, Leu-enkephalin, was

Table 1. Protein-related parameters of the CVO profiles from modeling the NR results shown in Fig. 1*A*

	500 nM KRAS-GppNHp	1 μM KRAS-GDP
KRAS surface density (lipids per protein)	100 ± 10	50 ± 4
Protein peak position from center of substrate-distal headgroups, Å	33 ± 4	38 ± 4
Protein CVO peak FWHM, Å	26 ± 6	28 ± 5

included as a control for the different levels of hydroxyl radical in each sample (36).

After footprinting, KRAS alone or complexed with nanodiscs (70:30 POPC:POPS) were digested with chymotrypsin and the modifications located by liquid chromatography–tandem mass spectrometry (LC-MS/MS). The modification level of each KRAS peptide was compared with the modification level of the reporter peptide at each histidine concentration (Fig. 1*C*). Excellent sequence coverage was obtained for KRAS; the only residues not identified in the peptide mapping were at positions 1 to 5 and 65 to 71. For each peptide, the two curves representing the sample and reporter peptides should overlap if bound and unbound states have identical solvent accessibilities. On the other hand, regions protected by membrane binding show deviations between the two curves (Fig. 1*C*). Although oxidized amino acids were found throughout the whole protein, only peptides corresponding to the HVR exhibited lower oxidation in the presence of nanodiscs, confirming direct interaction with the lipid bilayer. MS/MS analysis of these peptides identified M170, K176 to 179, K182, K184, and C185 with diminished oxidation levels in the presence of nanodiscs, indicative of their direct interaction with the lipid bilayer (Fig. 1*D*). No other surface-exposed amino acids exhibited altered oxidation levels in the presence of nanodiscs, providing further support for the specificity of the method and the interaction. These results clearly indicate that basic residues within the HVR directly mediate the predominant interaction of KRAS with the bilayer.

The KRAS G-domain: Membrane interactions are dynamic. To determine the orientation of KRAS on the membrane, we analyzed complexes of ^{15}N-labeled KRAS-GDP/GppNHp with nanodiscs by NMR. Rather surprisingly, the ^{15}N-transverse relaxation-optimized spectroscopy (TROSY) spectra (*SI Appendix*, Fig. S4 *A* and *B*) showed remarkably sharp and well-resolved peaks for a complex of 110 kDa (~89 kDa nanodiscs + 21.5 kDa ^{15}N-KRAS). We were able to identify NMR signals from HVR residues S171 and D173 to K179, indicating that this region is not persistently associated with the bilayer. A signal for residue K172 was not observed, probably owing to fast chemical exchange with bulk water at pH 7.4. Peaks corresponding to K180 to C185 were not observed when KRAS was bound to nanodiscs, most likely due to significant line broadening from strong interaction with the lipid bilayer. The expected increase in line widths was observed for the prenylated KRAS/nanodiscs complex (*SI Appendix*, Fig. S4*C*).

Small chemical shift perturbations (CSPs) were observed in the HVR (H166, M170, D173, K175, and K176) when comparing the spectra of prenylated and unprenylated KRAS-GppNHp in the presence of nanodiscs (*SI Appendix*, Fig. S4*D*). Small CSPs were also observed for residues S106, D108, and V109 in loop 7, a region that molecular dynamics (MD) simulations had previously implicated in transitions between exposed and occluded KRAS conformations on lipid bilayers (37). In comparison, CSPs in the HVR region of unprenylated KRAS-GppNHp with and without nanodiscs for residues M170, D173, and K175 (*SI Appendix*, Fig. S4*E*) were at least threefold smaller.

Data from 1D TROSY for rotational correlation times (TRACT) experiments (38) confirmed that KRAS-GDP were bound to nanodiscs (*SI Appendix*, Fig. S4 *F* and *G*). The rotational correlation time, τ_c, was determined to be 12.1 ns for free, unprenylated KRAS-GDP and 20.3 ns or 22.3 ns for KRAS-GDP on nanodiscs composed of 70:30 POPC:POPS or DMPC:DMPS, respectively. Based upon the correlation between τ_c values and molecular weights reported in ref. 38 and literature information compiled at http://sopnmr.ucsd.edu/biomol-tools.htm (*SI Appendix*, Fig. S5), the τ_c = 12.1 ns corresponds to a molecular weight of 26.8 kDa, which is close to 21.2 kDa, determined for ^{15}N-KRAS by mass spectrometry of the intact protein. The τ_c values of 20.3 ns and 22.3 ns for the KRAS-GDP:nanodisc complexes correspond to 48.1 kDa and 53.3 kDa, only half the expected value of 44 ns for a 110-kDa complex. Similar τ_c values to those obtained from 1D NMR TRACT were also estimated from ^{15}N T_1 and T_2 relaxation by using a rigid body assumption. Plots of ^{15}N T_1/T_2 relaxation ratios for individual residues identify flexible regions of the protein (*SI Appendix*, Fig. S6 *A* and *B*). These plots show a similar trend for the G-domain region with two dips centered around residues E62 (switch II) and V109 (loop 7). The HVR remains more mobile than the G-domain, as indicated by the lower T_1/T_2 ratio for HVR residues. Consistent with the conclusion obtained from NR, these results suggest dynamic states of the membrane-bound KRAS, in which the G-domain, tethered by the farnesylated/carboxymethylated HVR, rotates independently of the nanodisc and engages only transiently in interactions with the bilayer.

Sparsely populated membrane associated G-domain conformations identified by NMR-PRE. Previous NMR-PRE studies utilized [^{13}C]isoleucine- or ^{15}N-labeled KRAS chemically tethered to nanodiscs. In our current work, we used authentically prenylated and carboxymethylated ^{15}N-labeled KRAS, loaded with GDP or GppNHp. Ratios of the residue-specific spectral intensities, I/I_0, in the presence and absence of Gd^{3+} then provide information about surface areas of the protein in contact with the membrane. In this experimental design, the interpretation of the PRE effect is challenging, as both the Gd^{3+}-lipid chelate and KRAS can freely diffuse in the nanodiscs. However, by assuming that the Gd^{3+}-lipid chelate is evenly distributed within the bilayer, we can infer which residues are in proximity to the membrane. As a control, we measured changes in the PRE ratio of unprenylated KRAS-GppNHp in the presence of nanodiscs (*SI Appendix*, Fig. S6*C*). While there were minor decreases in PRE ratios for observable HVR residues, indicating weak interactions with the nanodiscs, no changes were observed within the G-domain, confirming the requirement of the farnesyl and carboxymethyl modification at C185 for stable membrane attachment.

In contrast, significant PRE changes were observed in similar experiments with authentically processed KRAS (Fig. 1*E* and *SI Appendix*, Fig. S6 *D* and *E*). Mapped onto the KRAS model, these data showed that the N-terminal β strands 1 to 3 and regions of α helices 2 to 5 are proximal to the membrane (Fig. 1*F*). As expected, the intensity of the signal decreases significantly from α5 through the HVR to the C terminus. In both the GDP and GppNHp bound states, NMR signals from G174 to K179 are completely lost in the presence of Gd^{3+}, suggesting that these residues are close to the bilayer. The r^{-6} distance dependence of the observed PRE ratios and the large paramagnetic effect at short distances suggest that KRAS samples sparsely populated states (39) in which the G-domain is located adjacent to the

membrane in addition to the highly populated states. Similarities in the PRE profiles for KRAS-GDP and KRAS-GppNHp indicated no apparent nucleotide dependence.

Membrane-distal and membrane-proximal conformations of the KRAS G-domain: Atomistic models from HADDOCK. HADDOCK (40, 41) was used to identify atomistic models that conform to NMR-PRE and NR measurements. First, we performed docking runs with NMR-PRE and R_g (radius of gyration) restraints to direct the structures toward matching the NR profiles for KRAS positioned off the membrane (Fig. 2*A*). Good agreement was obtained between the averaged profile from HADDOCK and the NR profile for membrane-distal conformations in which the G-domain is slightly displaced from the membrane. Such conformations of the KRAS G-domain were unlikely represented by any single HADDOCK result, and the algorithm identified an ensemble of such conformations with members of similar free energy.

Next, we generated fixed models of the KRAS G-domain at the membrane by using only the NMR-PRE data as restraints in HADDOCK (Fig. 2*B*). Docking KRAS-GDP to the membrane resulted in membrane-proximal states where the G-domain was in contact with the bilayer. Specifically, we identified two conformations that were already previously observed (15, 42). One family of conformations is characterized by the full exposure of the RBD binding site to bulk water, hereafter called the "exposed" conformation (15). These orientational states are within a broad and shallow basin on a free energy surface that shows little signs of corrugation, suggesting fast dynamic exchange. In the other, "occluded," conformation, the RBD binding site is adjacent to the membrane and unavailable for effector binding. In the context of the membrane, these conformations did not resemble those obtained from NR restraints. Taken together, this clearly suggests that KRAS configurations on the membrane, while dominated by membrane-distal conformations of the G-domain, also involve membrane-proximal conformations that are consistent with the NMR-PRE attenuation pattern.

Profiling the dynamic exchange of membrane-proximal conformations with coarse-grained MD simulations. HADDOCK models provided specific structures that are consistent with the NMR-PRE measurements. However, PRE data originate from an ensemble of conformations and representing them as a limited set of structures oversimplifies their dynamic interchange. MD simulations naturally provide an avenue to obtain information on the ensemble of conformations. We performed coarse-grained (CG) MD simulations to investigate membrane-proximal conformations of KRAS-GDP. Fig. 2*B* shows the free energy landscape of

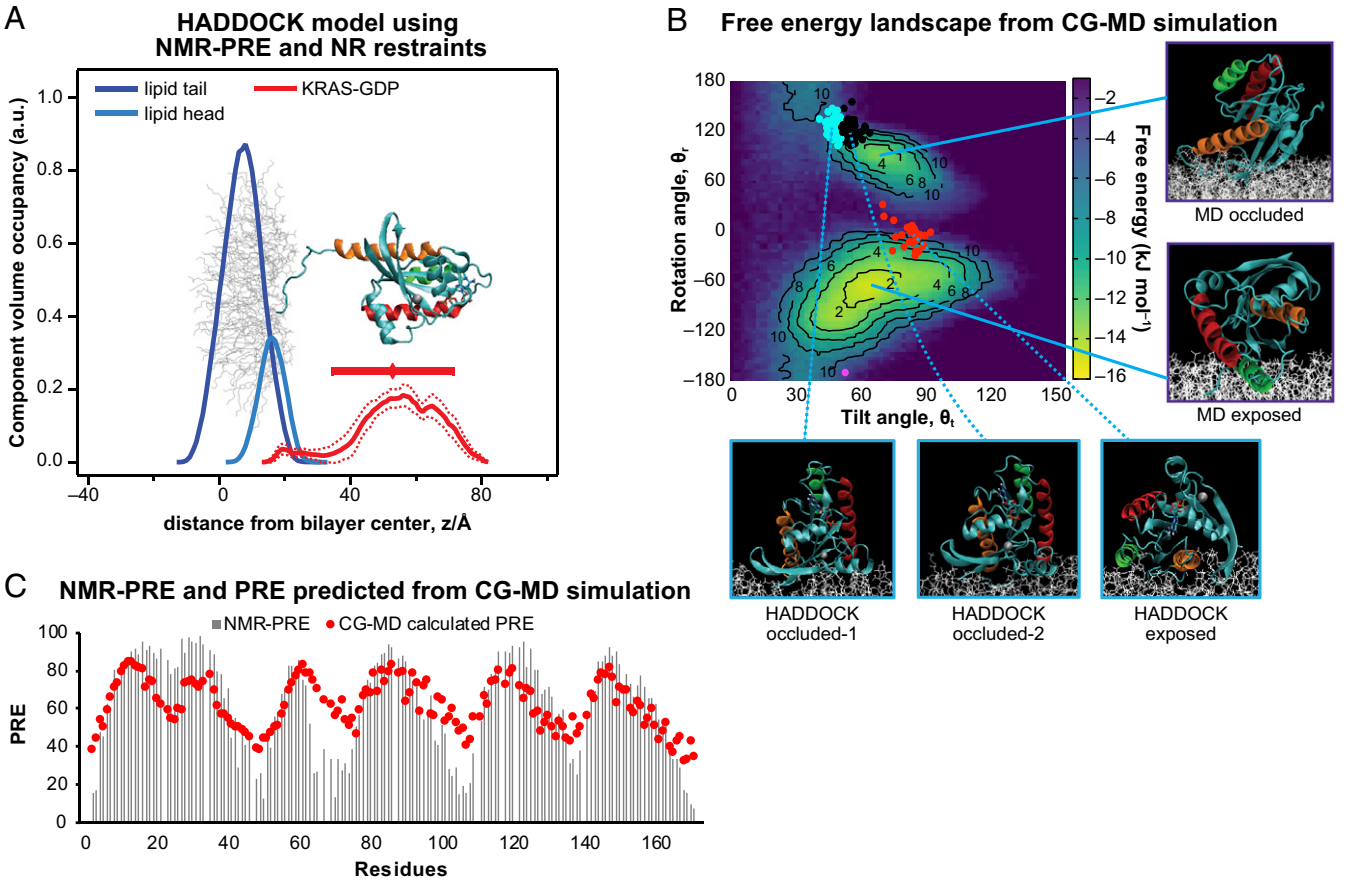

Fig. 2. Correspondence between experimental results and HADDOCK docking and CG MD simulation results of membrane-bound KRAS. (*A*) CVO profiles of the outer membrane monolayer leaflet and KRAS-GDP derived from HADDOCK with restraints and averaged over the 200 final structures. A representative structure is superimposed. A set of restraints favored G-domain orientations consistent with the NMR-PRE results and another, using the R_G (radius of gyration) feature in HADDOCK, approximated the distance of the G-domain from the membrane as determined by NR (indicated by the horizontal line with symbol for peak width and maximum, respectively). (*B*) Free energy landscape for membrane-bound KRAS that recapitulates the dynamics on a 70:30 POPC:POPS membrane obtained from MARTINI CG MD simulations. The tilt and rotation angles of KRAS with respect to the membrane (16) are based on 10 independent simulation replicas with a combined length of 1 ms. HADDOCK results (using only NMR-PRE restraints) in the same coordinate system are overlaid as red, black, magenta, and cyan dots. Insets here show averaged conformations for HADDOCK and CG MD-derived structures. α Helices are colored as described in the Fig. 1 legend. (*C*) Bar plot of measured NMR-PRE ratios for KRAS, overlaid with predictions (red dots) for the PRE effect from CG MD simulations for a mixture of 45% occluded and 55% exposed states and an offset distance of 0.45 nm.

these G-domain configurations with respect to the membrane as a function of two previously defined orientation parameters (16)—the tilt angle of the G-domain away from the bilayer normal, θ_t, and the azimuthal angle at which the tilt occurs, θ_r. This representation shows two dominant free energy basins that are consistent with those observed with all-atom MD simulations (43). The more extended basin is observed at $30° < \theta_t < 120°$ and $-160° < \theta_r < -20°$. Conformations within this basin resemble exposed conformations and show close contacts of α5 (orange helix), α4 (green helix), and α3 (red helix) of the G-domain with the membrane (Fig. 2*B*). As evidenced by the large dynamics in tilting, α3 and α5 can form transient interactions with the membrane through a "seesaw" mechanism in which α4 serves as the anchoring point. A second basin is narrower and localized at $60° < \theta_t < 90°$ and $50° < \theta_r < 100°$. Conformations within this basin are characterized by the direct interaction of β3 and β2 with anionic lipids and are populated by conformations where the RBD binding site is occluded.

We considered different population ratios of conformations from the MD-derived energy basins to compute the contributions of exposed and occluded populations that best reproduced the experimental PRE profile (Fig. 2*C* and see *SI Appendix*, *Materials and Methods* and Table S5). The best fit to the experimental PRE data represented a combination of 45% occluded and 55% exposed conformations, but the uncertainty of this ratio is large. While we were unable to determine statistically significant relative proportions of exposed and occluded populations, this analysis suggests a fast-dynamic exchange between the dominant membrane-proximal states.

The HADDOCK-generated configurations reside within and on the periphery of the CG MD free energy minima for the respective occluded and exposed conformational basins (Fig. 2*B*). We also analyzed five orientations of models obtained using the same HADDOCK docking algorithm. These configurations, shown in *SI Appendix*, Fig. S7*A*, are also observed as hits in our HADDOCK and CG MD simulation results, where we observed all of the previously published occluded and exposed conformations (42). Mapping of NMR-PRE intensity ratios onto representative CG MD exposed and occluded populations showed good correlations between the NMR-PRE data and the CG MD models, *SI Appendix*, Fig. S7*B*. Thus, two independent modeling approaches converge on the membrane-proximal conformations captured by NMR-PRE.

Effect of RAF1-RBD Binding on RAS Dynamics.

Positioning of the KRAS-GppNHp/RAF1-RBD complex on the membrane. The structure of the KRAS-GppNHp/RAF1-RBD complex at the membrane was characterized by NR. Given that neutrons interact differently with hydrogen (^{1}H) and deuterium (^{2}H), it is possible to separate contributions to the reflectivity from the hydrogenated and deuterated components of a complex. Accordingly, a complex of 500 nM hydrogenated KRAS-GppNHp and 500 nM deuterated RAF1-RBD was added to a preformed stBLM composed of 70:30 POPC:POPS. NR measurements of the stBLM were performed in H_2O and D_2O-based buffers before protein addition, during protein exposure, and after buffer rinse. The NR-derived CVO profiles (Fig. 3*A*) show that binding of RAF1-RBD to membrane-bound KRAS occurred in situ. Subsequently, within minutes after the buffer rinse, RAF1-RBD unbound from KRAS while the majority of KRAS proteins remained membrane-associated (*SI Appendix*, Fig. S8*A*), suggesting that dissociation of the KRAS/RAF1-RBD complex occurs faster than unbinding of KRAS from the membrane.

RAF1-RBD binding to KRAS occurred at a molar ratio of $1:(1.0 \pm 0.2)$ and the distance between the G-domain of KRAS and the center of the substrate-distal headgroups remained at 30 ± 3 Å (compare Figs. 1*A* and 3*A* and see *SI Appendix*, Table S3). A rigid-body modeling of the neutron data using the X-ray crystal structure of the KRAS/RAF1-RBD complex (PDB ID code 6VJJ) yields an excellent fit to the NR data assuming a unique orientation of the complex with respect to the membrane (Fig. 3*B* and *SI Appendix*, Fig. S8*B*). No additional broadening of the high-resolution structure during rigid-body modeling was required, indicating a narrowly distributed distance of the complex from the membrane. In this orientation, α2 and β1 to β3 of KRAS-GppNHp are parallel to the membrane and the RAF1-RBD loop between β3 and β4 (residues 101 to 108) points toward the membrane.

Changes in KRAS G-domain membrane association upon RAF1-RDB complexation. NMR-PRE experiments were performed with authentically processed ^{15}N-labeled KRAS-GppNHp in complex with RAF1-RBD bound to nanodiscs composed of 70:30 POPC:POPS (Fig. 3*C*). The data were noisier than those for KRAS-GppNHp alone owing to peak broadening upon RAF1-RBD binding. Overall, the PRE ratio pattern was similar to that observed with KRAS-GDP or KRAS-GppNHp by itself on nanodiscs.

Complementary experiments were performed with ^{15}N-labeled RAF1-RBD bound to unlabeled KRAS-GppNHp on nanodiscs (Fig. 3*D*). The most pronounced NMR-PRE effects on RAF1-RBD were observed on the loops between β1 and β2 (residues F61 to Q66) and between β3 and β4 (residues L101 to R111), consistent with the orientation determined with NR which predicted that the loop between β3 and β4 is proximal to the membrane. The interaction of these loops with the membrane is expected to be predominately hydrophobic and electrostatic, especially for residues L101 to R111 which include three hydrophobic and six cationic residues. A moderate NMR-PRE response was observed for β5 in the C-terminal region. NMR-PREs from KRAS and RAF1-RBD mapped onto the NR fitted model (Fig. 3*B*) are shown in Fig. 3*E*.

Modeling membrane-distal and -proximal conformations of the KRAS/RAF1-RBD complex using experimental restraints. As reported earlier for KRAS-GDP membrane docking (Fig. 2*A*), we used both NMR-PRE and R_g as HADDOCK restraints to derive atomistic models for KRAS-GppNHp/RAF1-RBD and determine averaged profiles for comparison with the NR profile. This resulted in a model of the complex where the G-domain and RBD are displaced from the membrane (Fig. 4*A*). Even with RAF1-RBD bound to the G-domain we did not observe conformations that simultaneously satisfied both the NR and NMR-PRE results. Similar to unbound KRAS, the KRAS/RAF1-RBD complex exhibits membrane-distal states, as observed in the NR results, along with membrane-proximal states identified in the NMR-PRE measurements.

Using only NMR-PRE restraints in HADDOCK docking runs, we observed that conformations in which the RBD binding site of the membrane-bound G-domain is partially exposed fit better than the "exposed" conformations identified with only KRAS on the membrane. We refer to such conformations as semiexposed (Fig. 4*B*). A decrease in the NMR-PRE signal intensity on α4 residues that are proximal to the membrane is consistent with an exposed conformation (Fig. 3*C*). While some initial high-energy structures from the HADDOCK docking results did contain exposed conformations, none were present in the final 200 structures (Fig. 4*B*). This is consistent with previous HADDOCK results on KRAS/ARAF-RBD which showed that semiexposed conformations represent the majority of the population of states with low energy, with only a minor population of exposed conformations (15). In the docking of KRAS/RAF1-RBD, energetic penalties to achieve exposed conformations were apparently significantly higher than for semiexposed conformations, and these penalties likely originate from the NMR-PRE restraints for RAF1-RBD, in particular for the RBD residues K65 and K106. Indeed, when repeating the same docking runs without the NMR-PRE restraints for RAF1-RBD we observed a mixture of semiexposed and exposed conformations in the final docked structures. These results suggest that the distributions of KRAS

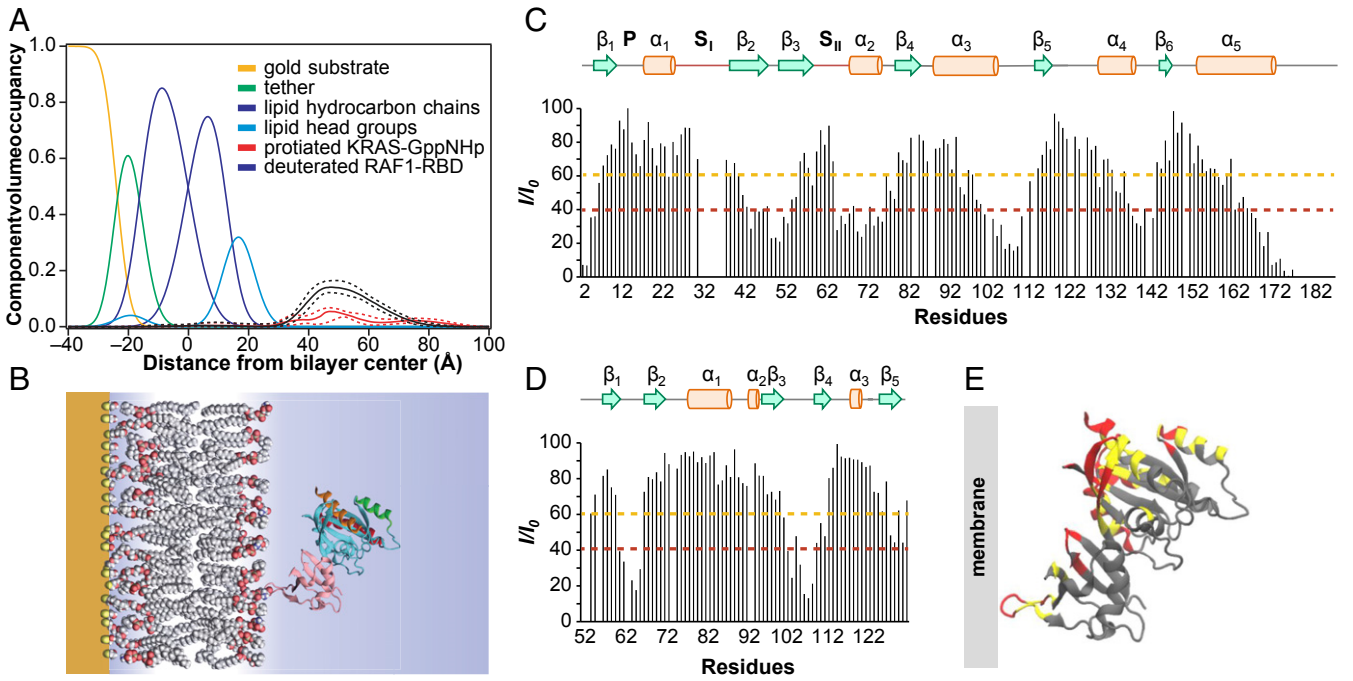

Fig. 3. NR and NMR data orient KRAS-GppNHp/RAF1-RBD on a membrane. (*A*) NR-derived CVO profiles of the KRAS-GppNHp/RAF1-RBD complex bound to an stBLM composed of 70:30 POPC:POPS. (*B*) Cartoon of the stBLM and the protein obtained by rigid-body modeling with the complex crystal structure (PDB 6VJJ). (*C* and *D*) NMR-PRE intensity ratios of ^{15}N-KRAS/RAF1-RBD and KRAS/^{15}N-RAF1-RBD in the presence of Gd^{3+}-labeled POPC:POPS nanodiscs, respectively. Unassigned and excluded residues within the G-domain (2–170) and RBD are left blank, see *SI Appendix* for further information. (*E*) NMR-PREs mapped onto the fitted structure in *B* using 40% (red) and 60% (yellow) cutoffs.

and KRAS/RAF1-RBD conformations from HADDOCK docking depend strongly on the number of restraints used.

Shifts in the membrane-proximal conformational population of KRAS upon binding to RAF1-RBD. Millisecond CG MD simulations of the KRAS-GppNHp/RAF1-RBD complex exhibited two major basins in the energy landscape as a function of the orientation angles θ_t and θ_r. The major basin containing the exposed conformations for KRAS observed earlier was preserved upon RAF1-RBD binding; however, occluded conformations in the other basin were slightly shifted with respect to θ_t, resulting in semiexposed conformations, as identified with HADDOCK. Representative structures are shown in Fig. 4*B*. The energy landscape looks quite similar to the one reported for KRAS/BRAF-RBD (16). The HADDOCK models showed significant similarity with the semiexposed ensemble of conformations obtained from CG MD. Thus, both computational approaches suggest a shift in membrane-proximal configurations toward semiexposed conformations in the KRAS/RAF1-RBD complex.

We observed that a dynamic ensemble of the bound KRAS/RAF1-RDB complex shifts toward the semiexposed state over time, reducing the amount of the exposed conformations to ~40%. This is consistent with the HADDOCK finding with NMR-PRE restraints that exposed conformations were unfavorable. The decrease of the exposed population in the presence of RAF1-RBD can be attributed to transient interactions of the effector with the membrane via a series of basic residues: K65 and K67 (in the loop between β1 and β2) and K106, K108, and K109 (in the loop between β3 and β4). These resides also show a significant intensity decrease in the NMR-PRE experiments confirming their interaction with the membrane. Fig. 4*C* shows a comparison between the experimental NMR-PRE intensities (gray bars) and computed average NMR-PREs (red dots) from MD simulations. Overall, the configurations captured by the CG MD simulations are in good agreement with the NMR data (see also *SI Appendix*, Fig. S9*A*). By varying the populations of exposed and semiexposed conformations, as before, we found that a ratio of 61%/39% semiexposed/exposed conformations best reproduced the NMR-PRE. Regardless of the uncertainty in this ratio, we conclude that relative population of these membrane-proximal conformations are altered by binding of the RAF1-RBD.

Discussion

Recruitment of RAF to the plasma membrane, by activated RAS, is a requirement for the activation of the MAPK signaling pathway. Defining KRAS's membrane-bound state is fundamental to understanding the initial steps in RAF activation. By using a combination of biophysical measurements and CG MD simulations we propose a model that describes how dynamic KRAS membrane interactions are important for RAF recruitment. Specifically, the NMR-PRE results reported here establish particular orientations of the G-domain on or near the membrane in line with earlier studies (15, 42), but they are not fully conclusive in distinguishing membrane-distal from -proximal states. Specifically, the complete quenching of HVR residues 174 to 185 and the incomplete quenching of specific G-domain residues (Fig. 1*E*), can be readily interpreted with two alternate models: 1) The G-domain is displaced from the membrane in a limited range of orientations or 2) The G-domain remains permanently membrane-bound with fast dynamic exchange between distinct orientational states. Both concepts are consistent with the observed NMR-PRE data, but model 1 is incompatible with the extensive body of simulation results while model 2 is contradicted by the NR, FPOP, and NMR data. However, a third possibility to interpret the NMR-PRE results is a dynamic directional exchange between membrane-proximal and -distal conformations.

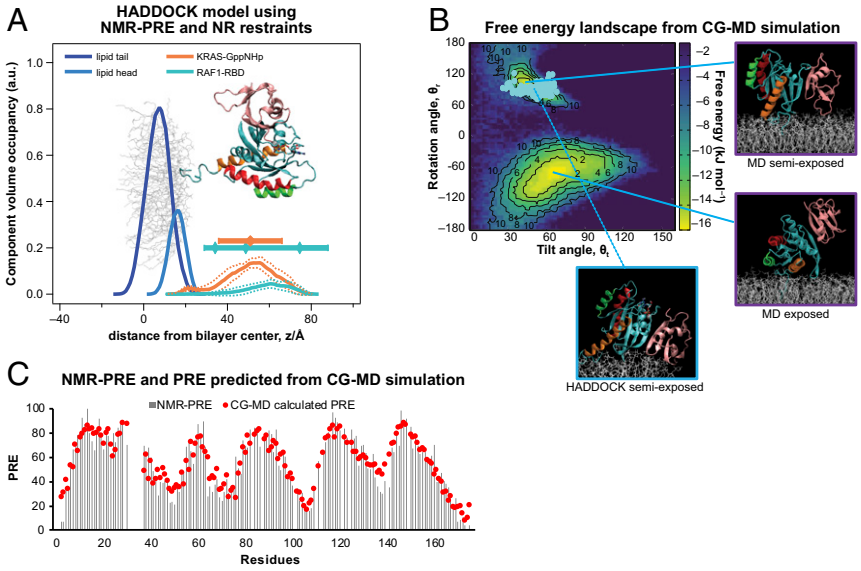

Fig. 4. Correlation of experimental results with HADDOCK docking and CG MD simulation results of the membrane-bound KRAS/RAF1-RBD complex. (*A*) CVO profiles of the outer membrane monolayer leaflet and the KRAS-GppNHp/RAF1-RBD complex, in which the constituent proteins are distinguished, as derived from HADDOCK with restraints. The CVO profile consists of an average over the 200 final structures. A representative structure is superimposed. A set of restraints favored protein orientations consistent with the NMR-PRE results and another, using the R_G (radius of gyration) feature in HADDOCK, approximated the distance of the protein complex from the membrane as determined by NR. Symbols and bars above the profile visualize the center positions and widths of the protein component profiles from NR (in which the RAF1-RBD component peaks in three distinct positions; see. Fig. 3*A*). (*B*) Free energy landscape recapitulating the dynamics of KRAS/RAF1-RBD bound to a 70:30 POPC:POPS membrane, as obtained from MARTINI CG MD simulations. The tilt and rotation angles of KRAS within the complex with respect to the membrane are based on 10 independent simulation replicas with a combined length of 1 ms. θ_t values are shifted by ∼−10° from those observed for membrane-bound KRAS alone (Fig. 2), brought about by steric collisions of RAF1-RBD with the membrane. HADDOCK results (using only NMR-PRE restraints) in the same coordinate system are overlaid as cyan dots for the predominant, semiexposed configuration of the G-domain on the membrane. Insets provide averaged conformations for HADDOCK and CG MD-derived structures with KRAS in cyan and RAF1-RBD in pink. (*C*) Bar plot of measured NMR-PRE ratios for KRAS within the complex with RAF1-RBD, overlaid with predictions (red dots) for the PRE effect from CG MD simulations for a mixture of 61% semiexposed and 39% exposed states and an offset distance of 0.286 nm.

The KRAS G-domain is found 36 ± 4 Å from the center of the substrate-distal headgroups (Fig. 1*A*)* and NR CVO profiles indicate that the membrane-distal conformation represents 90% of the ensemble (*SI Appendix*, *Methods*). This result is consistent with ^{15}N-TROSY and NMR TRACT, which indicate the membrane-proximal conformations are the minor species. Previous studies using fluorescence anisotropy demonstrated a high rotational mobility of membrane-anchored KRAS that was dominated by free rotation of the G-domain (44), consistent with our data. While there is experimental evidence that the G-domain makes weak and transient interactions with PIP_2-containing liposomes (45), FPOP footprinting on PC:PS bilayers showed no specific G-domain:membrane contacts, presumably because they occur on a submicrosecond timescale or remain below the level of detection. Our CG MD simulations and earlier computational work (21, 37, 43, 45–47) show clearly that the G-domain is mostly found associated with the membrane throughout the simulation timescales typically achieved, although a recent all-atom simulation identified KRAS states where the G-domain was not exclusively membrane-bound (17). Our HADDOCK docking results also reveal low-energy states in membrane-bound G-domain orientations that are consistent with the experimental NMR-PRE results. However, the fact that the bulk of the computational work (including our own) is not yet reconciled with experimental observation may reflect lingering deficiencies in the methodology. Empirical forcefields might not yet fully capture membrane electrostatics or there may be difficulties in exactly mimicking in computational simulations the experimental conditions that affect membrane-associated protein dynamics.

Remarkably, our analysis shows that energetically favorable orientations of the G-domain on the bilayer are preserved when the domain dissociates and assumes a membrane-distal conformation. This is revealed by the NMR-PRE results that show incomplete quenching of those G-domain residues in immediate contact with the bilayer in these orientations (Fig. 1*E*). Furthermore, the orientation of the G-domain in complex with the RAF1-RBD effector protein, identified in the NR and NMR-PRE results (Fig. 3), agrees with the membrane-bound G-domain orientations, both of the isolated G-domain and the KRAS/RAF1-RBD complex in computational models (Fig. 4). Specific G-domain residues that directly engage with anionic lipids (15, 21, 43, 45, 46, 48) may orient the membrane-proximal conformations, with correlation times below the microsecond range as the FPOP results suggest, that are preserved when the G-domain dissociates from the membrane. While our PRE-NMR data are consistent with this conclusion, spin labels such as Gd^{3+} have decreased sensitivity beyond 20 Å (49), and the G-domain may reside in alternate distal conformations that we are unable to detect. Finally, the rotational correlation time, τ_c, of small dissolved proteins is about 10 ns and presumably longer for the membrane-tethered G-domain. Since the lateral diffusion time across 10 Å—the distance between its membrane-proximal and -distal positions—is also in the 10-ns range, this provides a realistic scenario. We therefore suggest that dynamic directional exchange between rare membrane-proximal states and dominant membrane-distal states of the KRAS G-domain primes the protein toward productive contacts with its effectors or other RAS molecules in the assembly of nanoclusters.

*The center of the G-domain is then ∼25 Å from the bilayer surface, and the difference between the center-of-gravity positions of the G-domain as seen in NR and in atomistic MD simulations is ∼10 Å.

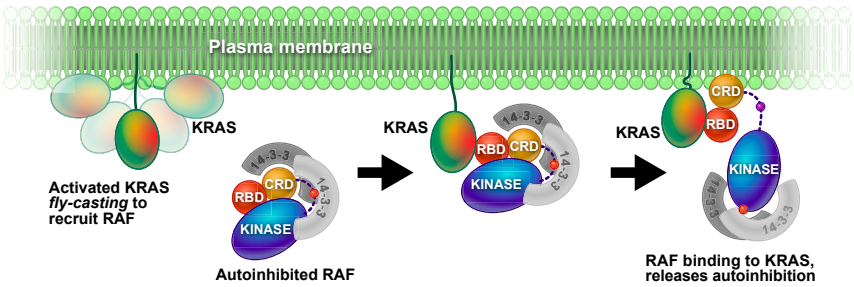

Fig. 5. Model of directional KRAS fly-casting, with the G-domain as bait for the RAF1-RBD, as a mechanism to recruit RAF to the membrane. Membrane-bound KRAS is dynamic, and both membrane-bound and membrane-tethered conformations coexist in fast dynamic exchange. Once freed from a transient, orientationally well-defined membrane-bound state, the KRAS G-domain, while firmly bound to the bilayer through its HVR, is dislodged from the surface under, at least approximate, conservation of the orientation defined by the membrane contact. This dynamic process facilitates the capture of the large effector protein which would not efficiently bind the small GTPase buried in the membrane. The autoinhibited RAF is modeled after a cryo-EM structure (10) in which the CRD is sequestered and the RBD, at the periphery of the RAF/14-3-3 complex, is available for interaction with KRAS.

KRAS dimers (4, 50–53) and nanoclusters (54–57) are important components in active signaling complexes. Dimerization of KRAS on a nanodisc with nucleotide-specific interfaces was recently identified, albeit with a weak affinity ($KD_{dim} \sim 600$ μM) (58). The α3-loop and C terminus of α5 region are close to the membrane in KRAS-GTPγS dimers, whereas KRAS-GDP dimers interact with the membrane via the C terminus of α5 and β1–β2–β3 (58). Our KRAS-GDP and GppNHp PRE-NMR data show no significant differences between the two nucleotide states, suggesting any dimer formation was below the level of detection. RAS nanoclusters are dynamic collections of protomers interacting with the membrane and with one another. KRAS shows a preference for planar membranes and clustering is favored on the plasma membrane with less curvature, in contrast to HRAS (59). While the conditions in our current study do not favor the formation of clusters, it is likely that on the plasma membrane when KRAS is in the distal conformation the G-domain is available to engage via all interfaces nanocluster assembly will be enhanced.

The dynamic exchange between membrane-distal and -proximal states is mediated by the disordered, flexible HVR. K180 to C185 associates tightly with the lipid bilayer and forms the primary membrane anchor within the HVR (Fig. 1*D* and *SI Appendix*, Fig. S4 *A* and *B*). The remainder of the HVR also makes strong contacts with the bilayer (Fig. 1*E* and *SI Appendix*, Fig. S6 *D* and *E*), although G174 to K179 are well-resolved in the NMR-TROSY spectra (*SI Appendix*, Fig. S4 *A* and *B*) and ^{15}N T_1/T_2 relaxation ratios for KRAS bound to nanodiscs indicated that the HVR retains significant flexibility (*SI Appendix*, Fig. S6*B*). These dynamic HVR:membrane interactions are of functional significance, as they mediate the diffusion on membranes (44, 60) and enable the rapid integration into signaling clusters (61–63). The recruitment of anionic lipid patches (47) by engagement of discrete lysines within the PBR with PS is essential for transitioning the HVR between different conformations (8). We propose these dynamic exchanges play a functional role in orienting KRAS to a membrane-proximal state for assembly into signaling clusters and effector engagement.

The KRAS/RAF1 RBD complex attains a well-defined orientation on the membrane (Fig. 4) that is similar to the semi-exposed state inferred for membrane-bound KRAS/ARAF-RBD from NMR-PRE studies (15). The exposed and semiexposed orientations of membrane-proximal KRAS/RAF1 RBD observed in the CG MD simulations are still attained even when the CRD is anchored to the membrane. Previous simulations (16) and recent NMR measurements (64) of the KRAS/RBD-CRD complex confirm these observations (*SI Appendix*, Fig. S9*B*). Positional information from our NR measurements places the KRAS/RAF1 RBD complex at a distance from the membrane surface similar to that of the isolated G-domain (Fig. 3). However, atomistic simulations of KRAS/RBD-CRD identify states where the G-domain is displaced from the membrane despite strong CRD–membrane interactions (17), confirming the dynamic nature of the G-domain relative to the membrane. RAS/RAF1-RBD complexation occurs at a rate of 10^7 $M^{-1}{\cdot}s^{-1}$, with a complex lifetime on the order of 50 to 100 ms (65). With 90% of the G-domain displaced from the bilayer and the lifetime of its membrane-bound states in the microsecond range, the RAF1-RBD is much more likely to engage KRAS in a membrane-distal state. Such disengagement from the bilayer may be a strict requirement for capture and recruitment of the RAF1 holoprotein to the much smaller, membrane-localized RAS protein.

In a directional fly-casting mechanism, the G-domain increases its interaction range considerably by engaging its effector as the bait. Transient membrane interactions orient KRAS such that its switch regions are accessible to capture RAF1 from solution by binding its RBD at a distance from the membrane surface, as schematically depicted in Fig. 5. This may be a requirement for facile effector activation, as RAS effector proteins are typically large, multidomain structures that might be incapable of binding small targets which are tightly membrane-embedded. The absence of any structural resolution of RBD in the recent cryo-EM structure of BRAF/MEK1/14-3-3 (10) suggests that it is dynamic in solution and available for recruitment by the membrane-distal KRAS G-domain. Recruitment of the G-domain back to a membrane-proximal state, mediated by fly-casting through the HVR, may facilitate the dephosphorylation of S259 of RAF1 (presumably by the membrane-associated SHOC2-MRAS-PP1 complex). Upon dephosphorylation and rearrangement of the 14-3-3 protomer the RAF1 CRD would be free to engage with the membrane and release the kinase domain from autoinhibition. While the substantiation of such an activation mechanism clearly requires further experimental and computational investigation, it provides an atomistic concept of KRAS4B membrane localization that is based upon extensive structural and computational results.

Materials and Methods

Protein production, nucleotide exchange, nanodisc preparation, SPR experimental conditions, stBLM preparations, and NMR experiments are fully described in *SI Appendix, Materials and Methods*.

NR. NR measurements were performed at the CGD-Magik reflectometer (66) at the NIST Center for Neutron Research. NR measurements of KRAS-GDP, KRAS-GppNHp, or a 1:1 complex of KRAS-GppNHp/deuterated RAF1-RBD on stBLM were performed as described previously (67) with minor changes. One-dimensional structural profiles of the substrate and the lipid bilayer along the lipid bilayer normal were parameterized using a continuous distribution model as described elsewhere (24).

FPOP Footprinting. FPOP was performed as described previously (68) and described in detail in *SI Appendix*. Specifically, unbound or nanodisc-bound KRAS, reporter peptide, H_2O_2, and variable levels of histidine to modulate the lifetime of the hydroxyl radicals were prepared and submitted to ~1,000 laser shots. The reporter was used to track the dosage (32, 36, 69). Each sample was prepared in triplicate. Following FPOP, samples were digested with chymotrypsin, LC-MS/MS separation, data analysis, and processing.

NMR Measurements. NMR data were collected at 25 °C on Bruker Avance III and Varian VNMRS spectrometers operating at 600, 800, or 900 MHz and equipped with cryogenic probes. Spectra were processed with NMRPipe (70) and analyzed/visualized with nmrDraw and NMRFAM-SPARKY (71). Further details are provided in *SI Appendix*.

Docking Simulations. Docking simulations were performed using HADDOCK (40, 41) with the NR and PRE data providing restraints. KRAS-GDP (PDB ID code 5TB5) and KRAS-GppNHp/RAF1-RBD (PDB ID code 6VC8) crystal structures were used. Docking simulations were performed as described previously (40, 41), with a complete description in *SI Appendix*.

MD Simulations and Computationally Derived PRE. All CG simulations were represented using the MARTINI 2.2 force field (72), and production runs were integrated using the GROMACS MD engine (version 5.1.4) with a recent update in CG parameters setup which allows higher efficiency in preserving the internal energy of the system (73). A full description of the simulated systems as well as the MD protocol is provided in *SI Appendix*.

Projected distances between every backbone MARTINI bead of the protein with respect to the surface of the membrane were used in order to back-calculate a PRE intensity profile. This MD-derived PRE was then compared to the experimentally derived PRE using a confidence analysis. A full description of the procedure is provided in *SI Appendix, Materials and Methods*.

Data Availability. All study data are included in the article and *SI Appendix*.

ACKNOWLEDGMENTS. Q.N.V. thanks Amanda Altieri and Mike Gregory for sharing their nanodisc-making expertise and Donghan Lee for providing the Excel worksheet to calculate τ_c from TRACT data. We thank members of the Frederick National Laboratory for Cancer Research (FNLCR) Protein Expression Laboratory for help with cloning (Carissa Grose, Jennifer Mehalko, and Vanessa Wall), *Escherichia coli* expression (John-Paul Denson), insect expression (Kelly Snead), and protein purification (John-Paul Denson, Shelley Perkins, and Mukul Sherekar). We thank Timothy Waybright, FNLCR, for validation of GppNHp exchange using high-pressure liquid chromatography analysis. Computing resources were made available by Los Alamos National Laboratory Institutional Computing. Research was performed in part at the National Institute of Standards and Technology (NIST) Center for Nanoscale Science and Technology. Certain commercial materials, equipment, and instruments are identified in this work to describe the experimental procedure as completely as possible. In no case does such an identification imply a recommendation or endorsement by NIST, nor does it imply that the materials, equipment, or instrument identified are necessarily the best available for the purpose. This project was funded in whole or in part with federal funds from National Cancer Institute (NCI), NIH Contract HHSN261200800001E and the Spatiotemporal Modeling Center at the University of New Mexico (NIH P50GM085273). This study made use of the National Magnetic Resonance Facility at Madison, WI, which is supported by NIH grant P41GM103399. Equipment was purchased with funds from the University of Wisconsin–Madison, the NIH (P41GM103399, S10RR02781, S10RR08438, S10RR023438, S10RR025062, and S10RR029220), and the NSF (DMB-8415048, OIA-9977486, and BIR-9214394). The mass spectrometry-based footprinting was conducted at the NIH facility at Washington University in St. Louis (Grant p41GM103422). This work has been supported in part by the Joint Design of Advanced Computing Solutions for Cancer (JDACS4C) program established by the US Department of Energy (DOE) and the NCI of the NIH. This work was performed under the auspices of the US DOE by Argonne National Laboratory under Contract DE-AC02-06-CH11357, Lawrence Livermore National Laboratory under Contract DE-AC52-07NA27344, Los Alamos National Laboratory under Contract DE-AC5206NA25396, Oak Ridge National Laboratory under Contract DE-AC05-00OR22725, and FNLCR under contract HHSN261200800001E. This work was supported by the US Department of Commerce (Award 70NANB17H299).

1. I. A. Prior, P. D. Lewis, C. Mattos, A comprehensive survey of Ras mutations in cancer. *Cancer Res.* **72**, 2457–2467 (2012).
2. J. F. Hancock, H. Paterson, C. J. Marshall, A polybasic domain or palmitoylation is required in addition to the CAAX motif to localize p21ras to the plasma membrane. *Cell* **63**, 133–139 (1990).
3. J. F. Hancock, A. I. Magee, J. E. Childs, C. J. Marshall, All Ras proteins are polyisoprenylated but only some are palmitoylated. *Cell* **57**, 1167–1177 (1989).
4. X. Nan *et al.*, Ras-GTP dimers activate the mitogen-activated protein kinase (MAPK) pathway. *Proc. Natl. Acad. Sci. U.S.A.* **112**, 7996–8001 (2015).
5. K. J. Cho, J. F. Hancock, Ras nanoclusters: A new drug target? *Small GTPases* **4**, 57–60 (2013).
6. K. J. Cho *et al.*, Inhibition of acid sphingomyelinase depletes cellular phosphatidylserine and mislocalizes K-Ras from the plasma membrane. *Mol. Cell. Biol.* **36**, 363–374 (2015).
7. S. J. Plowman, N. Ariotti, A. Goodall, R. G. Parton, J. F. Hancock, Electrostatic interactions positively regulate K-Ras nanocluster formation and function. *Mol. Cell. Biol.* **28**, 4377–4385 (2008).
8. Y. Zhou *et al.*, Lipid-sorting specificity encoded in K-Ras membrane anchor regulates signal output. *Cell* **168**, 239–251.e16 (2017).
9. H. Lavoie, M. Therrien, Regulation of RAF protein kinases in ERK signalling. *Nat. Rev. Mol. Cell Biol.* **16**, 281–298 (2015).
10. E. Park *et al.*, Architecture of autoinhibited and active BRAF-MEK1-14-3-3 complexes. *Nature* **575**, 545–550 (2019).
11. Y. Kondo *et al.*, Cryo-EM structure of a dimeric B-Raf:14-3-3 complex reveals asymmetry in the active sites of B-Raf kinases. *Science* **366**, 109–115 (2019).
12. D. Stokoe, S. G. Macdonald, K. Cadwallader, M. Symons, J. F. Hancock, Activation of Raf as a result of recruitment to the plasma membrane. *Science* **264**, 1463–1467 (1994).
13. L. C. Young *et al.*, SHOC2-MRAS-PP1 complex positively regulates RAF activity and contributes to Noonan syndrome pathogenesis. *Proc. Natl. Acad. Sci. U.S.A.* **115**, E10576–E10585 (2018).
14. E. M. Terrell, D. K. Morrison, Ras-mediated activation of the Raf family kinases. *Cold Spring Harb. Perspect. Med.* **9**, a033746 (2019).
15. M. T. Mazhab-Jafari *et al.*, Oncogenic and RASopathy-associated K-RAS mutations relieve membrane-dependent occlusion of the effector-binding site. *Proc. Natl. Acad. Sci. U.S.A.* **112**, 6625–6630 (2015).
16. T. Travers *et al.*, Molecular recognition of RAS/RAF complex at the membrane: Role of RAF cysteine-rich domain. *Sci. Rep.* **8**, 8461 (2018).
17. Z. L. Li, P. Prakash, M. Buck, A "tug of war" maintains a dynamic protein-membrane complex: Molecular dynamics simulations of C-Raf RBD-CRD bound to K-Ras4B at an anionic membrane. *ACS Cent. Sci.* **4**, 298–305 (2018).
18. S. Li, H. Jang, J. Zhang, R. Nussinov, Raf-1 cysteine-rich domain increases the affinity of K-Ras/Raf at the membrane, promoting MAPK signaling. *Structure* **26**, 513–525.e2 (2018).
19. W. K. Gillette *et al.*, Farnesylated and methylated KRAS4b: High yield production of protein suitable for biophysical studies of prenylated protein-lipid interactions. *Sci. Rep.* **5**, 15916 (2015).
20. D. J. McGillivray *et al.*, Molecular-scale structural and functional characterization of sparsely tethered bilayer lipid membranes. *Biointerphases* **2**, 21–33 (2007).
21. M. A. McLean, A. G. Stephen, S. G. Sligar, PIP2 influences the conformational dynamics of membrane-bound KRAS4b. *Biochemistry* **58**, 3537–3545 (2019).
22. H. Jang *et al.*, Mechanisms of membrane binding of small GTPase K-Ras4B farnesylated hypervariable region. *J. Biol. Chem.* **290**, 9465–9477 (2015).
23. B. Lakshman *et al.*, Quantitative biophysical analysis defines key components modulating recruitment of the GTPase KRAS to the plasma membrane. *J. Biol. Chem.* **294**, 2193–2207 (2019).
24. F. Heinrich, M. Lösche, Zooming in on disordered systems: Neutron reflection studies of proteins associated with fluid membranes. *Biochim. Biophys. Acta* **1838**, 2341–2349 (2014).
25. H. Nanda *et al.*, Electrostatic interactions and binding orientation of HIV-1 matrix studied by neutron reflectivity. *Biophys. J.* **99**, 2516–2524 (2010).
26. B. Akgun *et al.*, Conformational transition of membrane-associated terminally acylated HIV-1 Nef. *Structure* **21**, 1822–1833 (2013).
27. R. Eells *et al.*, Structural characterization of membrane-bound human immunodeficiency virus-1 Gag matrix with neutron reflectometry. *Biointerphases* **12**, 02D408 (2017).
28. P. Shekhar, H. Nanda, M. Lösche, F. Heinrich, Continuous distribution model for the investigation of complex molecular architectures near interfaces with scattering techniques. *J. Appl. Phys.* **110**, 102216 (2011).
29. B. P. Josey, F. Heinrich, V. Silin, M. Lösche, Association of model neurotransmitters with lipid bilayer membranes. *Biophys. J.* **118**, 1044–1057 (2020).
30. D. M. Hambly, M. L. Gross, Laser flash photolysis of hydrogen peroxide to oxidize protein solvent-accessible residues on the microsecond timescale. *J. Am. Soc. Mass Spectrom.* **16**, 2057–2063 (2005).
31. K. S. Li, L. Shi, M. L. Gross, Mass spectrometry-based fast photochemical oxidation of proteins (FPOP) for higher order structure characterization. *Acc. Chem. Res.* **51**, 736–744 (2018).
32. B. Niu, M. L. Gross, "MS-based hydroxyl radical footprinting: Methodology and application of fast photochemical oxidation of proteins (FPOP)" in *Mass Spectrometry-Based Chemical Proteomics*, W. A. Tao, Y. Zhang, Eds. (Wiley, 2019), pp. 363–416.
33. B. Niu, H. Zhang, D. Giblin, D. L. Rempel, M. L. Gross, Dosimetry determines the initial OH radical concentration in fast photochemical oxidation of proteins (FPOP). *J. Am. Soc. Mass Spectrom.* **26**, 843–846 (2015).
34. G. Xu, M. R. Chance, Hydroxyl radical-mediated modification of proteins as probes for structural proteomics. *Chem. Rev.* **107**, 3514–3543 (2007).
35. X. R. Liu, M. M. Zhang, D. L. Rempel, M. L. Gross, Protein-ligand interaction by ligand titration, fast photochemical oxidation of proteins and mass spectrometry: LITPOMS. *J. Am. Soc. Mass Spectrom.* **30**, 213–217 (2019).

36. B. Niu *et al*., Protein footprinting and X-ray crystallography reveal the interaction of PD-L1 and a macrocyclic peptide. *Biochemistry* **59**, 541–551 (2020).
37. P. Prakash, Y. Zhou, H. Liang, J. F. Hancock, A. A. Gorfe, Oncogenic K-Ras binds to an anionic membrane in two distinct orientations: A molecular dynamics analysis. *Biophys. J.* **110**, 1125–1138 (2016).
38. D. Lee, C. Hilty, G. Wider, K. Wüthrich, Effective rotational correlation times of proteins from NMR relaxation interference. *J. Magn. Reson.* **178**, 72–76 (2006).
39. G. M. Clore, J. Iwahara, Theory, practice, and applications of paramagnetic relaxation enhancement for the characterization of transient low-population states of biological macromolecules and their complexes. *Chem. Rev.* **109**, 4108–4139 (2009).
40. C. Dominguez, R. Boelens, A. M. Bonvin, HADDOCK: A protein-protein docking approach based on biochemical or biophysical information. *J. Am. Chem. Soc.* **125**, 1731–1737 (2003).
41. G. C. P. van Zundert *et al*., The HADDOCK2.2 web server: User-friendly integrative modeling of biomolecular complexes. *J. Mol. Biol.* **428**, 720–725 (2016).
42. Z. Fang *et al*., Inhibition of K-RAS4B by a unique mechanism of action: Stabilizing membrane-dependent occlusion of the effector-binding site. *Cell Chem. Biol.* **25**, 1327–1336.e4 (2018).
43. C. Neale, A. E. García, The plasma membrane as a competitive inhibitor and positive allosteric modulator of KRas4B signaling. *Biophys. J.* **118**, 1129–1141 (2020).
44. A. Werkmüller, G. Triola, H. Waldmann, R. Winter, Rotational and translational dynamics of ras proteins upon binding to model membrane systems. *ChemPhysChem* **14**, 3698–3705 (2013).
45. S. Cao *et al*., K-Ras G-domain binding with signaling lipid phosphatidylinositol (4,5)-phosphate (PIP2): Membrane association, protein orientation, and function. *J. Biol. Chem.* **294**, 7068–7084 (2019).
46. P. Prakash, A. A. Gorfe, Probing the conformational and energy landscapes of KRAS membrane orientation. *J. Phys. Chem. B* **123**, 8644–8652 (2019).
47. C. Neale, A. E. García, Methionine 170 is an environmentally sensitive membrane anchor in the disordered HVR of K-Ras4B. *J. Phys. Chem. B* **122**, 10086–10096 (2018).
48. Z. L. Li, M. Buck, Computational modeling reveals that signaling lipids modulate the orientation of K-Ras4A at the membrane reflecting protein topology. *Structure* **25**, 679–689.e2 (2017).
49. G. Otting, Protein NMR using paramagnetic ions. *Annu. Rev. Biophys.* **39**, 387–405 (2010).
50. C. Ambrogio *et al*., KRAS dimerization impacts MEK inhibitor sensitivity and oncogenic activity of mutant KRAS. *Cell* **172**, 857–868.e15 (2018).
51. P. Prakash *et al*., Computational and biochemical characterization of two partially overlapping interfaces and multiple weak-affinity K-Ras dimers. *Sci. Rep.* **7**, 40109 (2017).
52. H. Jang, S. Muratcioglu, A. Gursoy, O. Keskin, R. Nussinov, Membrane-associated Ras dimers are isoform-specific: K-Ras dimers differ from H-Ras dimers. *Biochem. J.* **473**, 1719–1732 (2016).
53. S. Muratcioglu *et al*., GTP-dependent K-Ras dimerization. *Structure* **23**, 1325–1335 (2015).
54. L. Li *et al*., Probing colocalization of N-Ras and K-Ras4B lipoproteins in model biomembranes. *ChemBioChem* **20**, 1190–1195 (2019).
55. L. Li *et al*., Dissociation of the signaling protein K-Ras4B from lipid membranes induced by a molecular tweezer. *Chemistry* **25**, 9827–9833 (2019).
56. R. Spencer-Smith *et al*., Inhibition of RAS function through targeting an allosteric regulatory site. *Nat. Chem. Biol.* **13**, 62–68 (2017).
57. Y. Zhou, P. Prakash, A. A. Gorfe, J. F. Hancock, Ras and the plasma membrane: A complicated relationship. *Cold Spring Harb. Perspect. Med.* **8**, a031831 (2018).
58. K. Y. Lee *et al*., Two distinct structures of membrane-associated homodimers of GTP- and GDP-bound KRAS4B revealed by paramagnetic relaxation enhancement. *Angew. Chem. Int. Ed. Engl.* **59**, 11037–11045 (2020).
59. H. Liang *et al*., Membrane curvature sensing of the lipid-anchored K-Ras small GTPase. *Life Sci. Alliance* **2**, e201900343 (2019).
60. J. K. Chung *et al*., K-Ras4B remains monomeric on membranes over a wide range of surface densities and lipid compositions. *Biophys. J.* **114**, 137–145 (2018).
61. S. Sarkar-Banerjee *et al*., Spatiotemporal analysis of K-Ras plasma membrane interactions reveals multiple high order homo-oligomeric complexes. *J. Am. Chem. Soc.* **139**, 13466–13475 (2017).
62. Y. Lee *et al*., High-throughput, single-particle tracking reveals nested membrane domains that dictate $KRas^{G12D}$ diffusion and trafficking. *eLife* **8**, e46393 (2019).
63. D. Goswami *et al*., Membrane interactions of the globular domain and the hypervariable region of KRAS4b define its unique diffusion behavior. *eLife* **9**, e47654 (2020).
64. Z. Fang *et al*., Multivalent assembly of KRAS with the RAS-binding and cysteine-rich domains of CRAF on the membrane. *Proc. Natl. Acad. Sci. U.S.A.* **117**, 12101–12108 (2020).
65. J. R. Sydor, M. Engelhard, A. Wittinghofer, R. S. Goody, C. Herrmann, Transient kinetic studies on the interaction of Ras and the Ras-binding domain of c-Raf-1 reveal rapid equilibration of the complex. *Biochemistry* **37**, 14292–14299 (1998).
66. J. A. Dura *et al*., AND/R: Advanced neutron diffractometer/reflectometer for investigation of thin films and multilayers for the life sciences. *Rev. Sci. Instrum.* **77**, 074301 (2006).
67. S. Shenoy *et al*., Membrane association of the PTEN tumor suppressor: Molecular details of the protein-membrane complex from SPR binding studies and neutron reflection. *PLoS One* **7**, e32591 (2012).
68. B. Niu *et al*., Incorporation of a reporter peptide in FPOP compensates for adventitious scavengers and permits time-dependent measurements. *J. Am. Soc. Mass Spectrom.* **28**, 389–392 (2017).
69. L. Shi, T. Liu, M. L. Gross, Y. Huang, Recognition of human IgG1 by Fcγ receptors: Structural insights from hydrogen-deuterium exchange and fast photochemical oxidation of proteins coupled with mass spectrometry. *Biochemistry* **58**, 1074–1080 (2019).
70. F. Delaglio *et al*., NMRPipe: A multidimensional spectral processing system based on UNIX pipes. *J. Biomol. NMR* **6**, 277–293 (1995).
71. W. Lee, M. Tonelli, J. L. Markley, NMRFAM-SPARKY: Enhanced software for biomolecular NMR spectroscopy. *Bioinformatics* **31**, 1325–1327 (2015).
72. S. J. Marrink, H. J. Risselada, S. Yefimov, D. P. Tieleman, A. H. de Vries, The MARTINI force field: Coarse grained model for biomolecular simulations. *J. Phys. Chem. B* **111**, 7812–7824 (2007).
73. D. H. de Jong, S. Baoukina, H. I. Ingólfsson, S. J. Marrink, Martini straight: Boosting performance using a shorter cutoff and GPUs. *Comput. Phys. Commun.* **199**, 1–7 (2016).